(Received 7 May 2024, Accepted 18 July 2024, Scheduled 14 August 2024)

Millimeter-Wave Quasi-Elliptic Filters in Groove Gap Waveguide Technology Using Overmoded Cavity with Spurious Coupling Suppression for Next-Generation SATCOM Applications

Rajni Kant[1,*], Deepak Ghodgaonkar[2], Abhishek Jindal[2], Parthasarathi Samanta[1], Hitesh Modi[1], and Praveen Kumar Ambati[1]

[1] *Space Applications Centre (SAC), ISRO, Ahmedabad, India*
[2] *Dhirubhai Ambani Institute of Information and Communication Technology (DA-IICT), Gandhinagar, India*

ABSTRACT: This paper addresses the issue of sidelobe imbalance due to spurious coupling in quasi-elliptic filters designed in groove gap waveguide (GGW) technology using TE_{102} overmoded cavity based resonator to realize the cross coupling in the cascaded quadruplet topology. The filter is designed at 38 GHz with 750 MHz bandwidth (1.97% fractional bandwidth) to demonstrate its potential as a narrowband, high-power output filter at mm-wave frequencies in next-generation high throughput satellites. The filter is designed for production yield avoiding any complex structures to realize the negative cross coupling and using an all-capacitive iris structure. Systematic studies have been performed to identify and mitigate the sidelobe imbalance issue, and a final design has been proposed with a very low (< 1 dB) sidelobe imbalance. The measured results of the realized hardware closely match simulated ones. The proposed design configuration is an ideal filter option for next generation SATCOM applications as it provides benefits of narrowband symmetrical frequency response with low insertion loss, sharp near band rejection, and high-power handling capability along with the benefits of gap waveguide technology in terms of ease of fabrication, low passive intermodulation (PIM) level, and low sensitivity towards surface imperfections and misalignment issues.

1. INTRODUCTION

In the new age of space-based high-throughput communication links, researchers and industrialists are migrating towards higher end of microwave frequency bands like the Ka-band and Q-band for higher data rate with a reduced hardware footprint. As more and more carriers and channels are being introduced, individual channel filter bandwidth is reduced, and ensuring sufficient inter-channel rejection between them becomes an important figure of merit for the overall system performance. Low insertion loss and high-power handling capability are the prime specifications of filters placed at the output of the high-power amplifiers (SSPAs, TWTAs). Over the past few years, an upward trend is observed in the output power required in next generation high-throughput satellites. As the fractional bandwidth per channel narrows down, complying with both the requirements of low insertion loss and high-power handling becomes increasingly difficult. Therefore, the next generation of high-power microwave filters poses a significant challenge to comply with the stringent requirements of narrow fractional bandwidth, high-power handling, and sufficient inter-channel rejection with as minimum footprint as possible. The breakdown and interference phenomenon of multipaction and PIM respectively associated with high-power components further add to the complexity of the filter design process.

Groove-gap waveguide (GGW) [1, 2] based microwave filters are potential candidates for such applications because of their unique properties like inherent immunity towards PIM [3], high-power handling capability with very low insertion loss [4, 5], and the insensitivity towards the fabrication tolerances. The main design principle stems from the concept of electromagnetic bandgap (EBG), where a wide stopband is created in between the region of a perfect electric conductor (PEC) and a perfect magnetic conductor (PMC), which is realized as an artificial magnetic conductor (AMC) with the help of a periodic bed of nails as shown in Fig. 1.

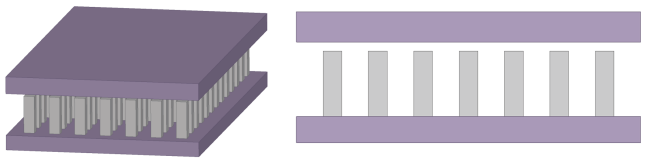

FIGURE 1. Electromagnetic bandgap (EBG) structure with PEC-AMC surface.

By introducing a rectangular groove inside the periodic bed of nails (as shown in Fig. 2) wave propagation for

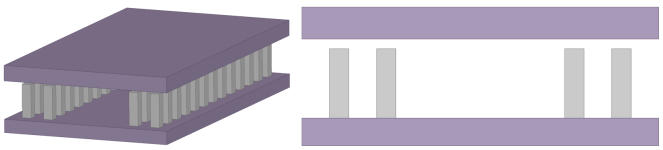

FIGURE 2. Groove gap waveguide.

* Corresponding author: Rajni Kant (pkantrajni@gmail.com).

the fundamental TE_{10} mode is allowed. Using this principle of electromagnetic bandgap, microwave filters are designed and reported in many research articles for both Chebyshev [6–8] and quasi-elliptic filtering functions, such as suspended-ridge [9], transversal coupling pillar [10], horizontally-polarized resonator [11], multi-slot cross-coupled filters [12], and vertically stacked multilayered filters [13–15]. One interesting way of generating transmission zeros in cascaded quadruplet topology using TE_{102} overmoded resonator is presented in [16]. It is a 4-pole quasi-elliptic filter at 38 GHz (Q-band) with cascaded quadruplet (CQ) topology. The TE_{102} overmoded cavity resonator introduces an extra 180° phase shift in the mainline which results in the multipath signal cancellation at the transmission zero frequencies. The design configuration is simple with all capacitive irises and does not use any complicated coupling structures which can potentially limit its high-power handling capability. However, the potential downside of such an overmoded cavity based GGW filter is the side-lobe imbalance, introduced by the spurious couplings. The mechanical model of the earlier reported filter is shown in Fig. 3. The simulated and measured frequency responses of the filter are shown in Fig. 4. The shift in the measured frequency response is because of the fabrication inaccuracies which can be easily mitigated by introducing tuning screws in the design or by strictly controlling the fabrication tolerances. The coupling matrix extraction method is used to analyze the simulated as well as measured frequency response which shows that the unwanted spurious coupling between the nonadjacent resonators (resonators 1–3, and 2–4) leads to the sidelobe imbalance around 11 dB. This work aims to identify the effect of different coupling structures in spurious coupling levels in the overmoded cavity resonator based CQ filters realized in groove-gap waveguide technology. The design process involves a thorough analysis to suppress this undesired coupling and provides a generic solution to this problem for GGW based overmoded CQ filters at high frequencies. This spurious coupling analysis and the suggested solution help to avoid additional poles (resonators) which would otherwise become inevitable to meet the rejection specifications in the presence of strong spurious couplings. These additional poles would not only increase the overall footprint and mass of the hardware, but also add to the insertion loss of the filter. In the case of narrow fractional bandwidth filter requirement in the high-throughput satellites, complying with the insertion loss requirement would become more challenging with higher-order filters. The analysis and mitigation method in this work, demonstrated with the help of a 4-pole overmoded CQ topology to compare with the electrical performance of the filter reported earlier in [16], however, is not limited to 4-pole overmoded CQ topology. The process can be applied to higher-order CQ filters using an overmoded cavity resonator based design in GGW technology by choosing the optimum coupling structures and their relative arrangements.

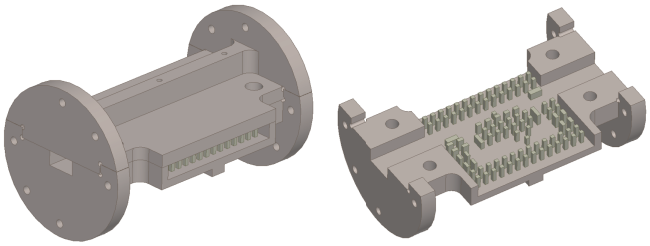

FIGURE 3. Groove Gap Waveguide filter with overmoded cavity resonator [16].

2. GROOVE GAP WAVEGUIDE TECHNOLOGY

Various dimensions of the periodic bed of metallic pins in the groove gap waveguide technology play a crucial role in microwave filter design using groove gap waveguide technology [17, 18]. These dimensions decide the overall stopband region created by these structures which is directly related to the spurious free bandwidth available for the filter design, and the RF power leakage which is reflected in the insertion loss of the filter. The dispersion diagram corresponding to an infinite two-dimensional periodic bed of nails is shown in Fig. 5, which shows a wide stopband from 25 to 50 GHz. Similarly, the dispersion diagram corresponding to the infinite one-dimensional groove gap waveguide structure is shown in Fig. 6, in which mode 5 is the propagating mode supported by the groove in-

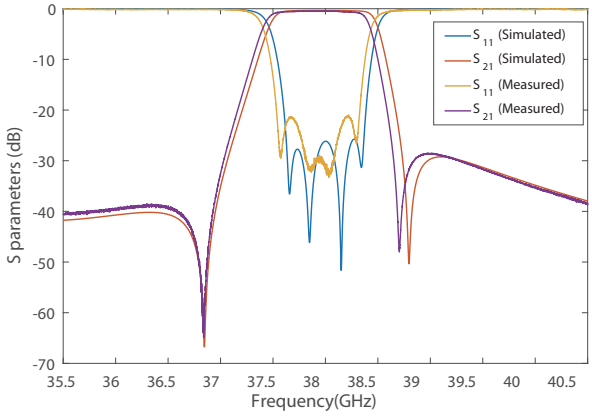

FIGURE 4. EM simulated vs. measured frequency response of the GGW filter with overmoded cavity resonator [16].

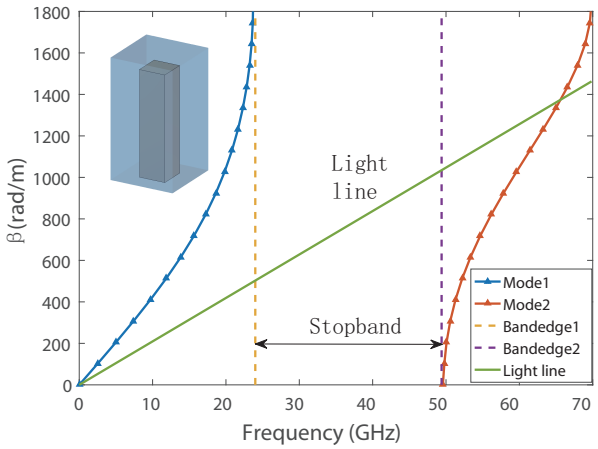

FIGURE 5. Dispersion diagram of the unit cell.

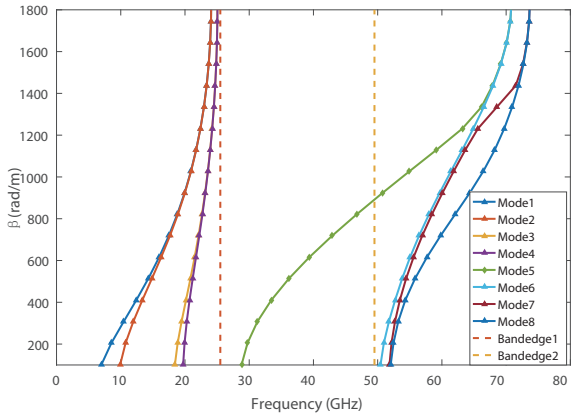

FIGURE 6. Dispersion diagram of the GGW array.

serted in between the periodic bed of metallic pins. The wave propagation along a rectangular groove gap waveguide is similar to the TE_{10} mode of wave propagation in conventional hollow rectangular waveguide. By selecting proper groove dimensions, TE_{10n} mode of cavity resonances can be established in groove gap waveguide technology which are used to design microwave filters. The EM model of a groove gap waveguide is shown in Fig. 7 which illustrates different dimensions of the structure, including the height of the pin (d), the gap between the top metal surface and the top surface of the pin (h), the periodicity of the metallic pins (p), cross-sectional width or diameter of the pins, and number of rows of pins in transversal direction. A summarized guideline is provided in [18] to choose these dimensions properly to ensure the optimum performance of the filter. Various dimensions of the groove gap waveguide used in this work are summarized in Table 1.

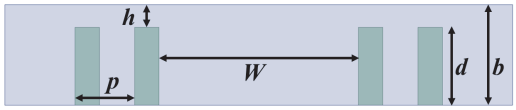

FIGURE 7. Various dimensions of groove gap waveguide.

TABLE 1. Groove gap waveguide dimensions.

Design Parameter	Values (in mm)
Waveguide width (W)	5.69
Waveguide height (b)	2.85
Pin height (d)	2.5
Gap between pins and metal wall (h)	0.35
Period of the pins (p)	1.7
Pin cross-section	0.7×0.7

3. FILTER SYNTHESIS AND EM SIMULATION

This work aims to investigate the effect of different coupling structures in the level of spurious coupling generated between non-adjacent resonators in an overmoded cavity based CQ filter at 38 GHz realized in groove gap waveguide, as a continuation of the work reported in [16]. The design and analysis in this work are based on a 4-pole quasi-elliptic filter with two

TABLE 2. Groove gap waveguide filter specifications.

Filter Parameter	Specifications
Centre frequency (GHz)	38
Bandwidth (MHz)	750
Insertion loss (dB)	≤ 0.5
Return loss (dB)	≥ 20
Rejection (dB) at	
(i) C.F ± 770 MHz	≥ 15
(ii) C.F ± 915 MHz	≥ 25
Input and Output Port	WR-22

transmission zeros (4-2-0 configuration). The filter specifications are given in Table 2 which are same as the specifications mentioned earlier in [16]. Although the earlier design complied with the specifications, the side-lobe imbalance was a major issue. In this work, since the study and mitigation of sidelobe imbalance is the major goal, filter specifications are unchanged from the previous one. However, with a balanced sidelobe, the filter can provide much better rejection for the specified rejection requirement. In case of more stringent rejection specification, the filter with a balanced sidelobe can comply with the specifications easily, while the filter with sidelobe imbalance may not comply with a 4-pole design and may call for a higher-order filter design (5-pole or 6-pole).

An important factor for selecting 4-pole CQ filter to study the spurious coupling and sidelobe imbalance is its topology. From the theory of filter synthesis, it is evident that for similar return loss and sidelobe levels in the synthesized frequency response, the mainline coupling values towards the centre of the filter topology are relatively smaller in higher-order filters than the mainline coupling values in case of a lower-order filter. In case of 4-pole CQ filters, the mainline coupling values around the CQ structure are relatively higher leading to larger iris openings in the physical structures which in turn results in higher level of undesired spurious couplings between non-adjacent resonators. However, in case of 5 or 6-pole CQ filters, the topology can be chosen in such a way that the CQ structure is closer to the centre of the topology (as shown in Fig. 8) where mainline coupling values are relatively smaller than the 4-pole CQ case, and consequently the spurious coupling level is relatively lower which it has less severe impact on the sidelobe imbalance. Hence, in this work, the analysis is carried out in a 4-pole CQ filter, but the process can be easily extended to higher-order CQ filters using an overmoded cavity in groove gap waveguide technology. The negative cross-coupling between the non-adjacent

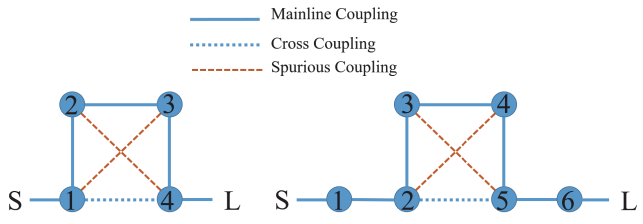

FIGURE 8. CQ topology in a 4-pole filter vs. 6-pole filter.

resonators [19] is realized by using phase reversed magnetic field in a TE_{102} overmoded cavity resonator [20] as shown in Fig. 10 (signals from resonator 1 to resonator 4 via mainline coupling (1-2-3-4) and via non-adjacent cross-coupling (1–4) are in opposite phase because of the additional 180° phase introduced in the TE_{102} cavity resonator). Hence, both TE_{101} and TE_{102} cavity mode resonances are used in the filter design. Fig. 9 shows TE_{101} and TE_{102} mode cavities in groove gap waveguide technology.

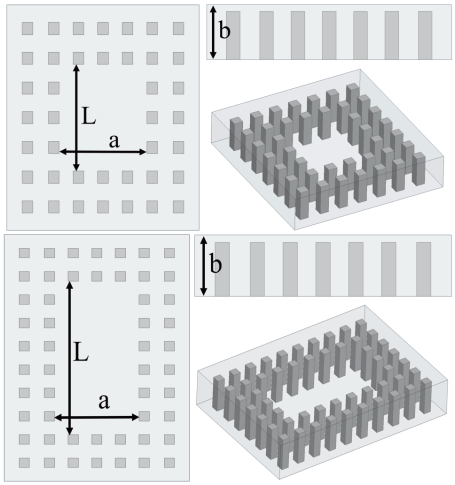

FIGURE 9. TE_{101} and TE_{102} cavity resonators in GGW technology.

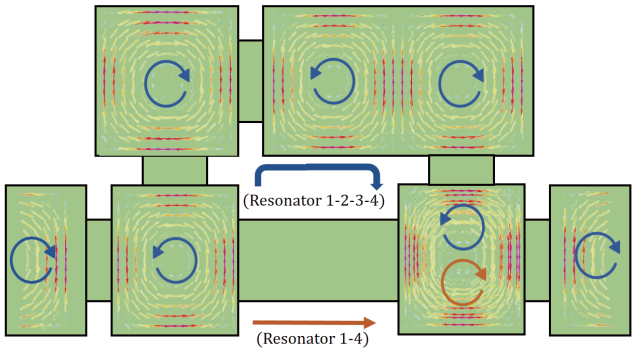

FIGURE 10. Realization of cross-coupling using phase-reversed magnetic field in a TE_{102} overmoded cavity.

The coupling matrix corresponding to the 4-pole CQ filter is synthesized in a MATLAB® routine following the procedure of generalized coupling matrix synthesis method [21, 22], and the resulting coupling matrix is

$$M = \begin{bmatrix} 0 & 1.16 & 0 & 0 & 0 & 0 \\ 1.16 & 0 & 1.03 & 0 & -0.15 & 0 \\ 0 & 1.03 & 0 & 0.84 & 0 & 0 \\ 0 & 0 & 0.84 & 0 & 1.03 & 0 \\ 0 & -0.15 & 0 & 1.03 & 0 & 1.16 \\ 0 & 0 & 0 & 0 & 1.16 & 0 \end{bmatrix}$$

The analytical formula for the resonance frequency of TE_{mnl} mode in a rectangular cavity resonator with metal side walls is given by

$$f_{mnl} = \frac{c}{2\pi\sqrt{\mu_r \epsilon_r}} \cdot \sqrt{\left(\frac{m\pi}{a}\right)^2 + \left(\frac{n\pi}{b}\right)^2 + \left(\frac{l\pi}{L}\right)^2} \quad (1)$$

where c is the speed of light in vacuum; m, n, l are numbers of half-cycles of electric field in X, Y, and Z directions, with X-axis being aligned with the broad wall dimension (a) of the waveguide, Y-axis being aligned with the side wall dimension (b) of the waveguide, and Z-axis being aligned with the direction of propagation (L) along the length of the waveguide. Since the wave propagation in groove gap waveguide is similar to the TE_{10} mode of wave propagation in rectangular waveguide, the resonance frequencies of the TE_{101} and TE_{102} mode cavities in groove gap waveguide technology can be approximated using this analytical expression by varying the length of the resonant cavity in a parametric sweep. However, for a more accurate estimation of the cavity length, systematic parametric sweep is run in Ansys HFSS® software using the eigen-mode solver. The resulting plot between the resonance frequency and the cavity length is shown in Fig. 11 and Fig. 12.

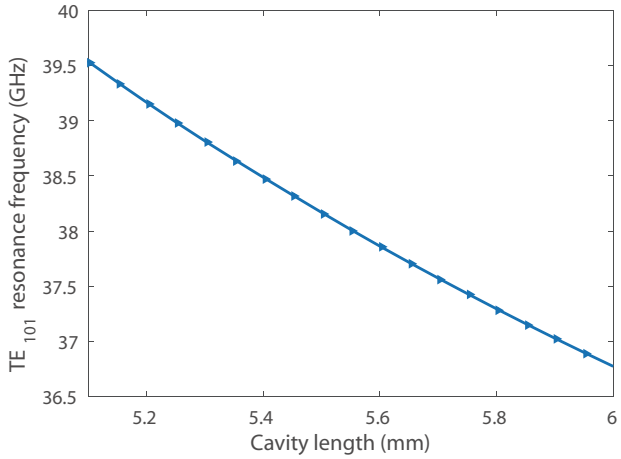

FIGURE 11. TE_{101} cavity resonance frequency vs cavity length in GGW technology.

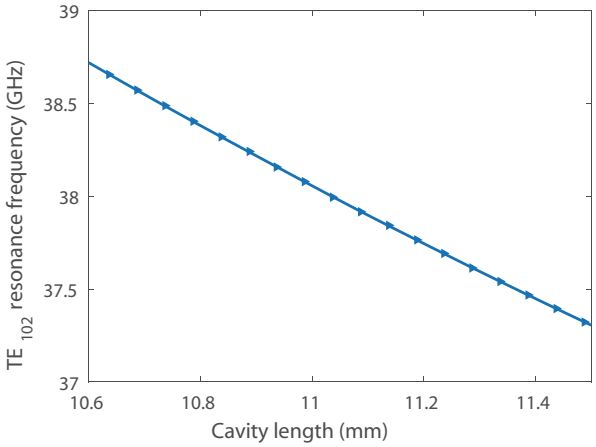

FIGURE 12. TE_{102} cavity resonance frequency vs cavity length in GGW technology.

The initial dimensions of the resonators are then estimated from the plot. To characterize the coupling values, reflection group-delay method [23] is used. For the external coupling characterization (J_{S1}), one-port single peak reflection group delay simulations are carried out to find out the external quality factor (Q_E) as well as the value of the external couplings from the following equations

$$Q_E = \frac{\omega_0 \Gamma_{d0}}{4} \tag{2}$$

$$J_{S1} = \sqrt{\frac{2}{\pi \cdot \Delta f \cdot \Gamma_{d0}}} \tag{3}$$

where ω_0 is the center frequency of the filter, Δf the bandwidth of the filter, and Γ_{d0} the peak value of the reflection group delay when the phase transition frequency is aligned with the center frequency as shown in Fig. 13.

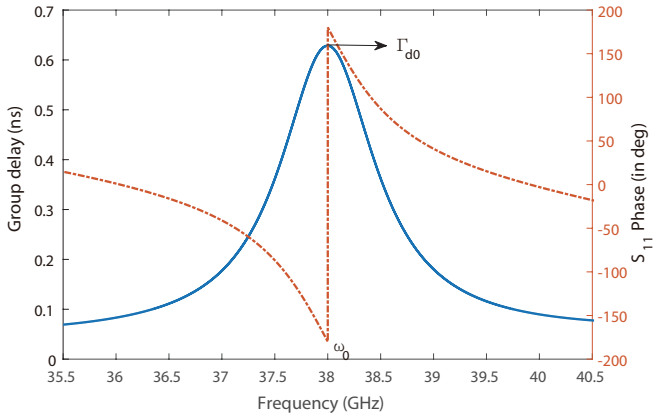

FIGURE 13. Single-port single peak reflection group delay plot for external coupling characterization.

In a similar manner, J_{12} and J_{23} can be characterized by the reflection group delay method in single-port driven modal EM simulation. For J_{12}, single-port two-peak reflection group-delay method (with two resonators) is used, where J_{12} is given by

$$J_{12} = \frac{\omega_2 - \omega_1}{\omega_0} \cdot \frac{\omega_0}{\Delta\omega} \tag{4}$$

where ω_0 is the center frequency; $\Delta\omega$ is the bandwidth; and ω_2 and ω_1 are the phase transition frequencies in the single-port two peak reflection group delay plot in balanced condition (as shown in Fig. 14). For J_{23} single-port three peak reflection group delay method is used, and J_{23} is given by

$$J_{23} = \frac{\omega_{2'} - \omega_{1'}}{\omega_0} \cdot \frac{\omega_0}{\Delta\omega} \tag{5}$$

where ω_0 is the center frequency; $\Delta\omega$ is the bandwidth; and $\omega_{2'}$ and $\omega_{1'}$ are the zero crossing frequencies of S_{11} phase in the single-port three peak reflection group delay plot (as shown in Fig. 15) in balanced condition.

In the EM model, these coupling values are achieved by varying the height of the coupling posts and calculating the coupling

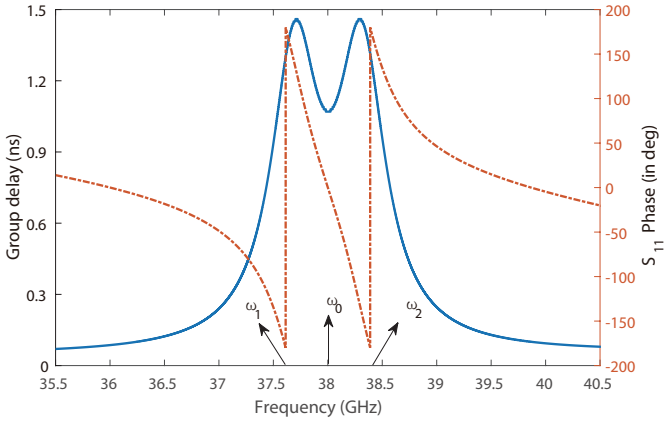

FIGURE 14. Single-port two peak reflection group delay plot for J_{12} coupling characterization.

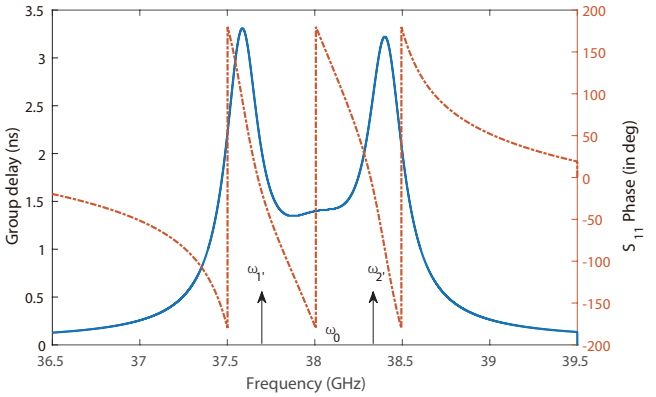

FIGURE 15. Single-port three peak reflection group delay plot for J_{23} coupling characterization.

values from the single-port reflection group delay plots using Equations (3)–(5).

Once the J_{S1}, J_{12}, and J_{23} coupling values are characterized from the input side, J_{4L} and J_{34} coupling values are characterized in a similar manner (single-peak and two-peak reflection group delay method) from the output side. Finally, the J_{14} non-adjacent coupling is characterized by using eigen-mode analysis in Ansys HFSS®. From the theory of synchronously tuned resonators, the value of the coupling is given by —

$$|K| = \frac{f_1^2 - f_2^2}{f_1^2 + f_2^2} \tag{6}$$

where f_1 and f_2 are the two eigen-mode frequencies of the coupled resonator structure in the EM solver.

In overmoded cavity based CQ filter, the phase cancellation is provided by the phase reversal of the magnetic field in the TE_{102} overmoded cavity resonator. So, it is important to note that, unlike conventional CQ filters where the cross couplings between the non-adjacent resonators are opposite in nature as compared to the mainline couplings, in overmoded CQ filters, the coupling between the non-adjacent resonators (J_{14} in this case) and the mainline coupling are of the same nature. Hence, in the eigen-mode analysis it must be ensured that the sign of this coupling value is same as that of the mainline coupling with

the help of the electromagnetic field patterns. The variation of the J_{14} coupling with the coupling post height is shown in Fig. 16. Because of the loading effect on the resonators, the center frequency gets shifted (the variation is as shown in Fig. 16), and the necessary adjustments in the resonance frequencies of the resonators need to be implemented.

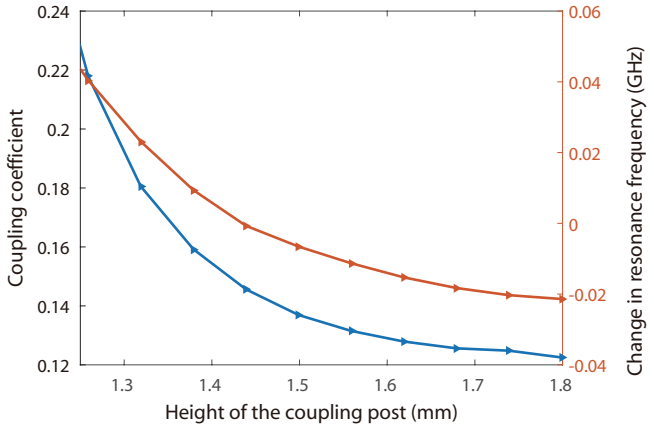

FIGURE 16. J_{14} coupling value vs. height of the coupling post.

For all of these coupling characterizations, the resonators which are not considered in the characterization process must be detuned to eliminate their impact on the characterization. After characterizing the resonances and couplings from the eigen-mode analysis and reflection group-delay method, the full 3-D electromagnetic simulation is run to optimize the final frequency response.

4. ANALYSIS AND MITIGATION OF SPURIOUS COUPLING

In order to study the origin and the effect of spurious couplings in the sidelobe imbalance of the frequency response, coupling matrix extraction technique is used, and the extracted values are verified in the equivalent circuit model in the presence of the spurious coupling. Once the level of spurious coupling and its origin are identified, its impact on the sidelobe imbalance is studied systematically in the EM simulation. It is observed in the EM simulations that the locations of the capacitive irises at the beginning and end of the CQ structure (in this case the J_{S1} and J_{4L} coupling posts) play a crucial role in the spurious coupling and sidelobe imbalance level. To verify the observation, 6 case studies are carried out in which the location of the external coupling structures (J_{S1} and J_{4L}) are varied to study the boundary cases. The relative positions of the J_{S1} and J_{4L} coupling structures are shown in Fig. 17 with respect to their zero positions. Zero position is defined as the position, when the edges of the coupling posts are closest to the inner resonators (resonator 2 and 3) of the CQ structure (with 1 mm gap from the bed of pins for fabrication feasibility). X and Y denote the shift of the J_{S1} and J_{4L} coupling structures with respect to the zero position in mm. With respect to the zero position, the offsets that move the coupling structures away from the other resonators are defined as positive offsets (in the figure, direction

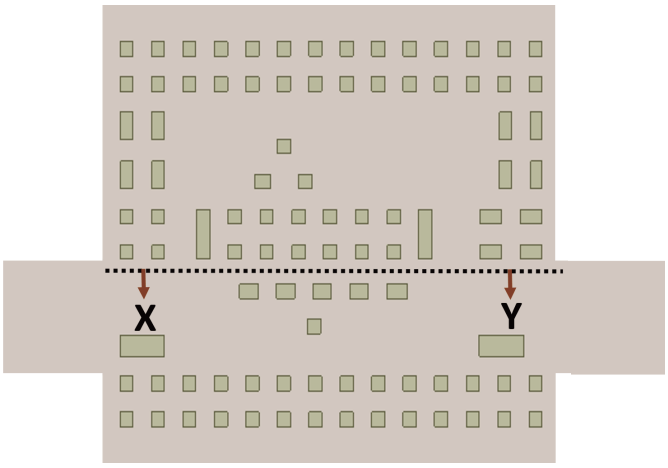

FIGURE 17. Relative locations of external coupling structures with respect to their zero position.

of positive X and positive Y are shown). The 6 case studies comprise the boundary cases as described

$$
\begin{aligned}
Case1: &\ X = 0,\ Y = 0.\\
Case2: &\ X = +0.645,\ Y = +0.645.\\
Case3: &\ X = +2.045,\ Y = +2.045.\\
Case4: &\ X = +2.690,\ Y = +2.690.\\
Case5: &\ X = 0,\ Y = +2.690.\\
Case6: &\ X = +2.690,\ Y = 0.
\end{aligned}
$$

The case studies are chosen in a way where the coupling posts are gradually shifted from the inner resonators of the CQ structure to the periodic bed of nails on the other side, and two diagonal cases are considered to include all the boundary cases.

The EM simulated frequency responses of these 6 cases are shown in Fig. 18, and the extracted coupling values from the s2p files are summarized in Table 3. From these frequency responses it is observed that from cases 1 to 4 as the external coupling posts are shifted away from the inner resonators of the CQ structure (resonators 2 and 3), the sidelobe imbalance gradually

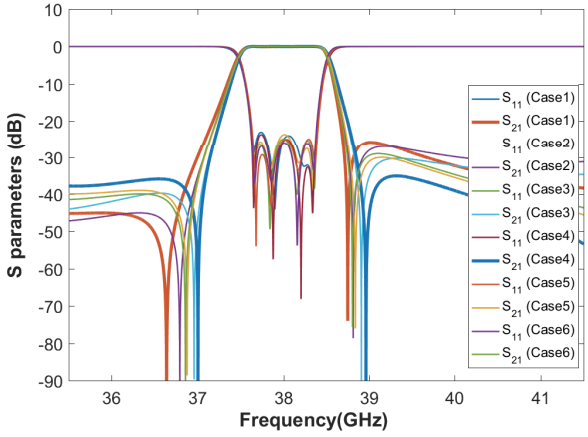

FIGURE 18. EM simulated frequency response of the GGW filter in 6 different cases.

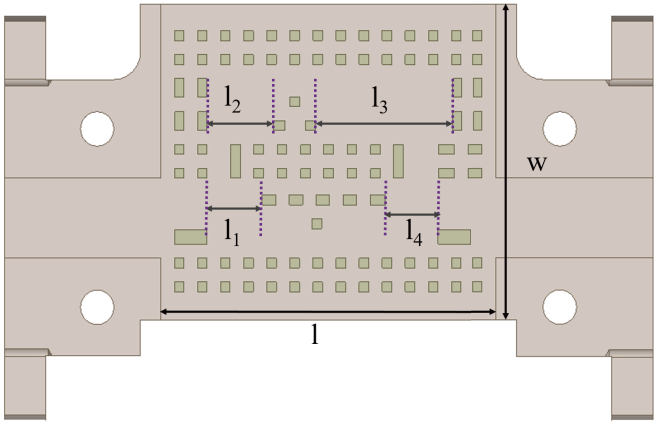

FIGURE 19. Mechanical model of the overmoded CQ filter with resonator lengths.

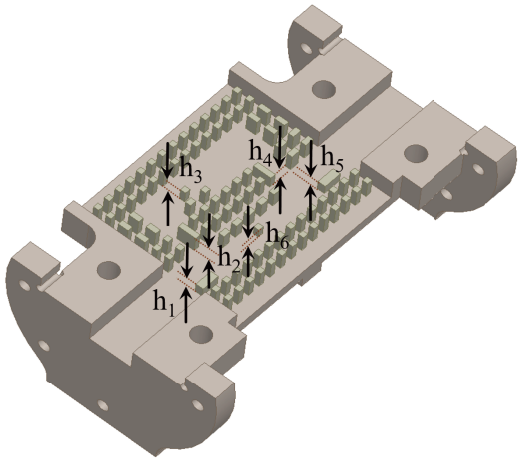

FIGURE 20. Mechanical model of the overmoded CQ filter with coupling heights.

decreases. The sidelobe imbalance can be solely attributed to the spurious coupling levels only when the filter performance is fully optimized, and the in-band return loss is good (preferably more than 20 dB). Since the return loss bandwidth in all of these cases is the same and the in-band return loss more than 20 dB, it provides a fairground to justify sidelobe imbalance in terms of the level of spurious couplings only. Fig. 18 shows that in case 4, the sidelobe imbalance is minimum (less than 1 dB) which is also justified by the extracted value of the spurious couplings between non-adjacent resonators in Table 3, whereas the worst-case sidelobe imbalance occurs in case 1 (around 19 dB) when the level of the spurious couplings is the maximum. The trend in the level of spurious couplings in these 6 cases shows that when the external coupling posts are kept closer to the inner resonators, the level of spurious couplings is higher than the location where the coupling structures are kept away from the inner resonators. To understand these phenomena, filter's physical structure is studied in detail in each of these cases. In each of these cases, the cavity width (a) is 5.69 mm; cavity height (b) is 2.85 mm; the thickness and length of the J_{S1} and J_{4L} coupling posts are 1 mm and 2.4 mm, respectively; the thickness and length of the J_{12} and J_{34} coupling posts are 0.7 mm and 2.4 mm, respectively; the cross-sections of the J_{23} and J_{14} coupling pins are 0.7 mm $\times$ 0.7 mm; the overall length (l) of the filter (excluding port lengths) is 24.8 mm; and the overall width (w) is 22.49 mm. Fig. 19 and Fig. 20 show the resonator lengths (l_i, $i = 1, 2, 3, 4$) and height of the coupling posts (h_i, $i = 1, 2, 3, 4, 5, 6$), respectively, whose values are summarized in Table 4. From Table 4, it is evident that as the coupling posts at the input and output of the CQ structure (J_{S1} and J_{4L}) are shifted away from the inner resonators (resonator 2 and 3), the height of the mainline coupling posts closer to these posts (h_2 and h_4) increases monotonically from case 1 to case 4. Fig. 21 explains this phenomenon with the help of the two extreme cases (case 1 and case 4). The field intensity (H_z and E_y, as per the coordinate system shown in Fig. 21) at the J_{12} iris location increases when the external coupling post is shifted away. Since the field strength is more, the iris opening should be decreased to realize the same amount of coupling bandwidth. As a consequence, the height of the coupling posts increase. Since the mainline iris openings decrease, the undesired spurious coupling between non-adjacent resonators also decreases which leads to a reduction in sidelobe imbalance. In cases 5 and 6 which are the diagonal cases, whenever the external coupling post is kept closer to one of the inner resonators (resonator 2 in case 5 and resonator 3 in case 6), the height of the mainline

TABLE 3. Extracted coupling matrix in different cases.

	Case 1	Case 2	Case 3	Case 4	Case 5	Case 6
J_{S1}	1.156	1.161	1.157	1.164	1.170	1.167
J_{12}	1.029	1.031	1.033	1.036	1.032	1.020
J_{23}	0.829	0.829	0.840	0.835	0.834	0.829
J_{34}	1.033	1.034	1.035	1.036	1.035	1.031
J_{4L}	1.167	1.165	1.163	1.164	1.162	1.159
J_{14}	−0.141	−0.142	−0.150	−0.147	−0.151	−0.152
J_{13}	0.134	0.085	0.035	0.018	0.074	0.082
J_{24}	0.134	0.085	0.035	0.018	0.074	0.082
m_{11}	0.039	0.091	0.044	−0.051	−0.012	0.031
m_{22}	−0.118	−0.048	−0.023	−0.043	−0.085	−0.067
m_{33}	−0.139	−0.061	−0.039	−0.050	−0.109	−0.070
m_{44}	−0.083	−0.027	−0.014	−0.069	−0.004	0.009

TABLE 4. Filter dimensional details in different cases.

	Case 1	Case 2	Case 3	Case 4	Case 5	Case 6
h_1	1.415	1.699	1.692	1.406	1.411	1.405
h_2	2.054	2.220	2.366	2.377	2.057	2.38
h_3	1.712	1.708	1.698	1.703	1.699	1.666
h_4	1.593	1.678	1.780	1.783	1.784	1.548
h_5	1.427	1.723	1.692	1.401	1.401	1.426
h_6	1.368	1.396	1.364	1.329	1.339	1.359
l_1	4.079	4.105	4.091	4.059	4.080	4.069
l_2	4.881	4.869	4.873	4.875	4.877	4.874
l_3	10.224	10.164	10.117	10.122	10.126	10.245
l_4	3.989	3.977	3.919	3.887	3.896	4.022

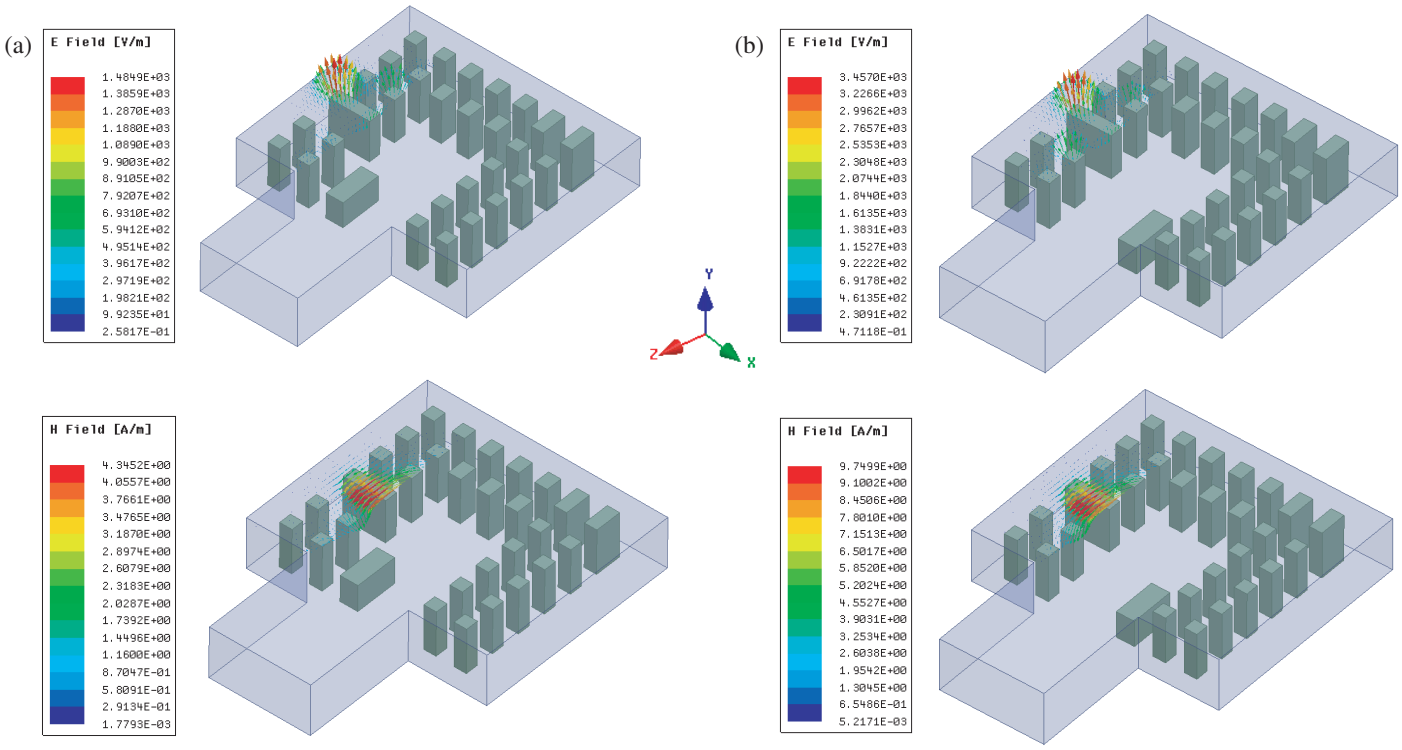

FIGURE 21. Field intensity at the J_{12} iris location in (a) case 1 (worst-case) and (b) case 4 (best-case).

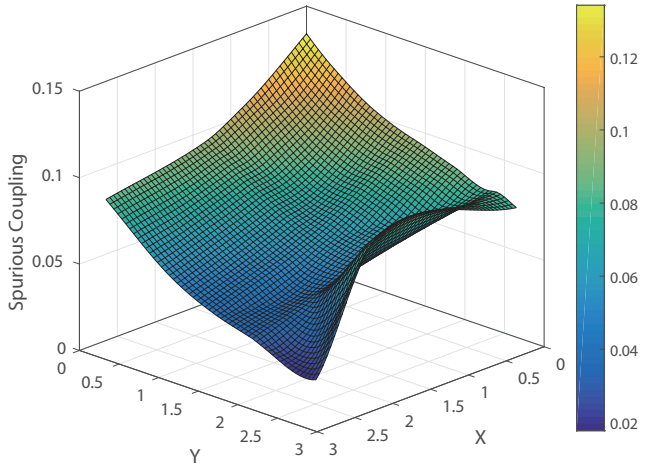

FIGURE 22. Level of spurious coupling as a function of the relative locations of the external coupling structures.

coupling post closer to the external coupling post (h_2 in case 5 and h_4 in case 6) decreases which results in an increase of the spurious coupling level, but lies somewhere in between the extreme cases (case 1, worst-case and case 4, best-case). The resonator lengths are almost the same in all of these cases and do not have any significant role in sidelobe imbalance. The heights of the external coupling posts (h_1 and h_5) and cross-coupling post (h_6) also do not have any significant impact on the spurious coupling level since only the iris openings of the mainline couplings at the interior of the CQ structure decide the level of spurious coupling between non-adjacent resonators. The variation in the height of these external coupling posts comes from the electric field distribution of the TE_{10}-like mode in GGW technology. Towards the centre of waveguide, the field intensity (H_x and E_y, as per the coordinate system shown in Fig. 21) is maximum, and relatively small iris opening is required to achieve the required coupling bandwidth, and hence in cases 2 and 3 where these posts are closer to the center of the waveguide, the height of these coupling posts are more. These trends rationally justify the initial observation that the level of spurious couplings depends on the location of the external coupling structures. To verify this trend further, 20 more EM simulations are carried out with different locations of the external coupling structures within these 6 corner cases since 6 sample points are not enough to bring out the overall distribution of the spurious coupling level as a function of the location of the external coupling structures. A bi-cubic interpolation is then carried out on these sample data in MATLAB®, and the resulting plot between the spurious coupling and the relative locations of external coupling structures is shown in Fig. 22. The 2-D colormap of the same plot is shown in Fig. 23, which clearly depicts the trend of decreasing level of spurious coupling in the diagonal direction from the lower left corner ($X = 0, Y = 0$, closest to resonators 2 and 3) to the upper right corner ($X = +2.69, Y = +2.69$, farthest to resonators 2 and 3). It is evident that the sidelobe imbalance is a function of the level of spurious couplings between non-adjacent resonators which depends on the iris openings of the mainline couplings inside the CQ structure. A very small variation in the level of spurious coupling (0.02 to 0.12) can lead to a sidelobe imbalance variation of 1 dB to 19 dB which can have some serious impact on the performance of filters, es-

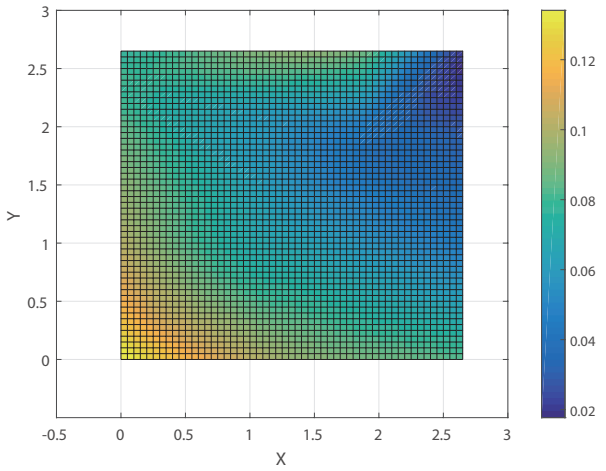

FIGURE 23. 2-D projection of the spurious coupling as a function of the relative locations of the external coupling structures.

pecially in the cases with relatively small number of poles and fractional bandwidth. The final EM model along with the field pattern (at 38 GHz) is shown in Fig. 24 which depicts the magnetic field of the TE_{10} mode-like cavity resonances in groove gap waveguide technology.

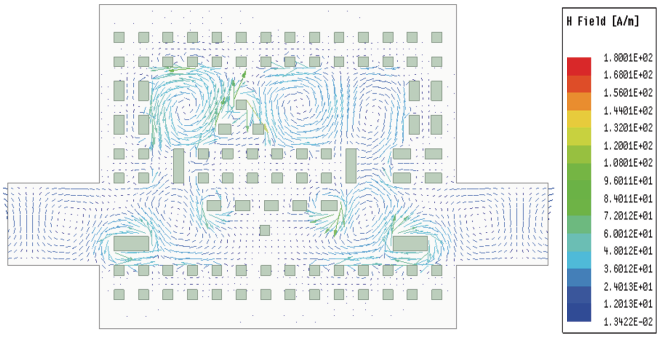

FIGURE 24. H-field distribution in final EM model (with improved side-lobe imbalance) at center frequency.

5. DESIGN CONSIDERATIONS FOR SPACE APPLICATIONS

Groove gap waveguide based filters are excellent candidates for high-power output filters in space applications at millimeter wave frequencies. But before these cavity resonators based filters can be used in space environment, some factors related to the high-power handling capability and frequency shifts need to be considered which are discussed in this section.

5.1. Frequency Shift Due to Thermal Cycles

Space-based hardware experiences a wider range of temperatures. In operating conditions, the temperature range is usually controlled in the range $-10°C$ to $+65°C$ by proper thermal design. The volume of the cavity resonator changes with this temperature drift, and the overall effect is captured in the frequency drift of the cavity resonators. For different materials, this shift is different as it depends on the coefficient of thermal expansion of the material. But in filter design, a more convenient metric is used to account for the frequency shift which is known as ELFD or Equivalent Linear Frequency Drift [24]. It gives us a number that can be used to calculate the overall frequency drift of the filter. This extra drift can be then adjusted in the filter design bandwidth to meet the required specifications of passband flatness and out-of-band rejections over operating temperature range. For example, if the GGW-based filter is fabricated with aluminium, the frequency drift of a filter at 38 GHz can be calculated for a temperature range of $-10°C$ to $+90°C$ (self-heating included) as follows

$$\begin{aligned} ELFD &= 24\,\text{ppm}/°\text{C} \\ f_0 &= 38000\,\text{MHz} \\ \Delta T &= 100°\text{C} \\ Frequency\ drift &= ELFD \cdot f_0 \cdot \Delta T \\ &= \frac{24 \cdot 38000 \cdot 100}{1000000}\,\text{MHz} \\ &= 91.2\,\text{MHz} \end{aligned}$$

So, the design bandwidth of the filter has to be symmetrically increased by 91.2 MHz to meet all the required specifications over temperature.

5.2. Frequency Correction due to Hard Vacuum Environment

The resonance frequencies of the cavity resonators in a cavity-based filter depend on the dielectric constant of the medium that fills the cavities. During the development of the cavity filters in the clean room, the tuning and testing process happen in ambient environment with controlled temperature and relative humidity. But during the on-orbit operating condition, the filter is exposed to a hard vacuum environment whose dielectric constant is slightly different from the dielectric constant in the clean room test environment. Consequently, a frequency shift occurs when the filter is tested in a thermo-vacuum chamber in near vacuum condition. To compensate this frequency shift, the filter is designed or tuned at a slightly lower center frequency in the clean room so that in vacuum condition the actual specifications are met. The calculation of the modified center frequency (approximate) is described below.

In the case of air, the relationship between the dielectric constant and pressure is approximately linear. So, if we can calculate the pressure change from vacuum condition to the ambient clean room condition, we can calculate the frequency change by calculating the change in the dielectric constant. Since the relationship between dielectric constant and pressure is linear, we can write

$$\frac{\epsilon_r - \epsilon_{r,vacuum}}{\epsilon_{r,air} - \epsilon_{r,vacuum}} = \frac{P_{total} - P_{vacuum}}{P_{air} - P_{vacuum}}$$

During the thermo-vacuum testing, the pressure is less than 10^{-3} mbar, and in the actual space environment with hard vacuum, the pressure level can go lower than 10^{-12} mbar. So, P_{vacuum} can be neglected compared to the regular atmospheric

pressure, and the equation can be written as

$$\epsilon_r = \epsilon_{r,vacuum} + \frac{\epsilon_{r,air} - \epsilon_{r,vacuum}}{P_{air}} \cdot P_{total}$$

P_{total} comprises two factors. One factor is the standard atmospheric pressure at the test location, and the other factor comes from the relative humidity of the test environment. So, the total pressure is calculated as

$$P_{total} = P_{atm} + P_{relativehumidity}$$

From the Clausius-Clapeyron equation, the pressure due to relative humidity (in mbar) can be calculated as

$$P_{relativehumidity} = 6.11 \cdot \exp\left(\frac{17.27 \cdot T}{237.3 + T}\right) \cdot \frac{RH}{100}$$

where RH is the relative humidity in percentage, and T is the temperature in °C. The dielectric constant of vacuum is 1 ($\epsilon_{r,vacuum} = 1$), and at sea-level dry air's dielectric constant and pressure are given by

$$\begin{aligned} \epsilon_{r,air} &= 1.0006; \\ P_{air} &= 1013.3\,\text{mbar}; \end{aligned}$$

the epsilon is calculated as follows

$$\epsilon_r = 1 + \frac{0.0006}{1013.3}\left(P_{atm} + 6.11 \cdot \exp\left(\frac{17.27 \cdot T}{237.3 + T}\right) \cdot \frac{RH}{100}\right)$$

Now, the ratio of the modified frequency (required during the clean lab testing in the presence of ambient pressure, temperature, and relative humidity) and the original frequency (required in the vacuum condition) can be expressed as

$$\frac{f_{modified}}{f_{vacuum}} = \frac{1}{\sqrt{\epsilon_r}}$$

For example, for a GGW-based filter at 38 GHz (required at vacuum), the modified centre frequency is calculated as

$$\begin{aligned} T &= 24.7°\text{C}. \\ RH &= 44.4\%. \\ \epsilon_r &= 1.000608. \\ \frac{f_{modified}}{f_{vacuum}} &= \frac{1}{\sqrt{\epsilon_r}} = 0.999696. \\ f_{modified} &= 37.98845\,\text{GHz}. \end{aligned}$$

So, the filter needs to be tuned at 37.98845 GHz (approximately 12 MHz away) in ambient conditions.

5.3. Multipaction Analysis

Multipaction is a high-power RF breakdown phenomenon in vacuum. When high-power signal flows through the filter structure, high-energy primary electrons pull out secondary electrons from the metal surface upon impact with the walls of the cavities and irises. With adequate impact energy, the secondary electron yield (SEY) may become greater than 1 (if the colliding electron has too little energy, the SEY will be less than 1. If it has too much energy then the secondary electron emitted will be buried inside the metal itself, and the SEY will again be less than 1. In between these two extreme limits, SEY can become more than 1). For a given band of incident energy and angle of incidence of the primary electrons, the SEY is different for different metals. For the multipaction to sustain, the SEY should be greater than 1. Along with the SEY greater than 1, if the gap crossing time is an odd multiple of the half-cycle of the applied RF signal, secondary electron resonance takes place which generates noise and in extreme cases can permanently damage the physical structure of the filter resulting in permanent degradation of the RF performance, and eventually the failure of the RF link. In order to predict the multipaction threshold, multipaction analysis of the newly designed GGW-based filter (with improved sidelobe imbalance) is carried out using CST Spark3D tool®, and the result is shown in Fig. 25 which shows a multipaction threshold around 13.25 kW. A detailed study on methods to improve the peak-power handling capability in groove gap waveguide technology using horizon-

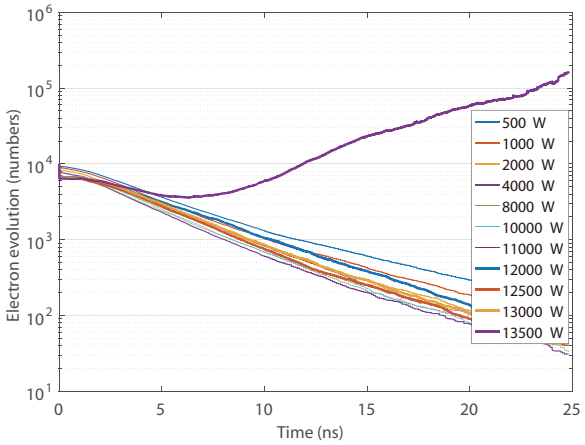

FIGURE 25. Multipaction analysis of the GGW-based filter with improved sidelobe imbalance.

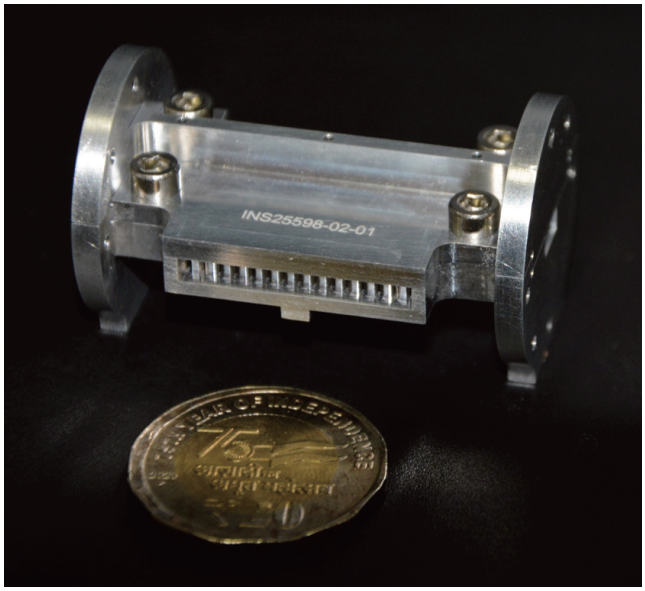

FIGURE 26. Fabricated hardware in assembled condition.

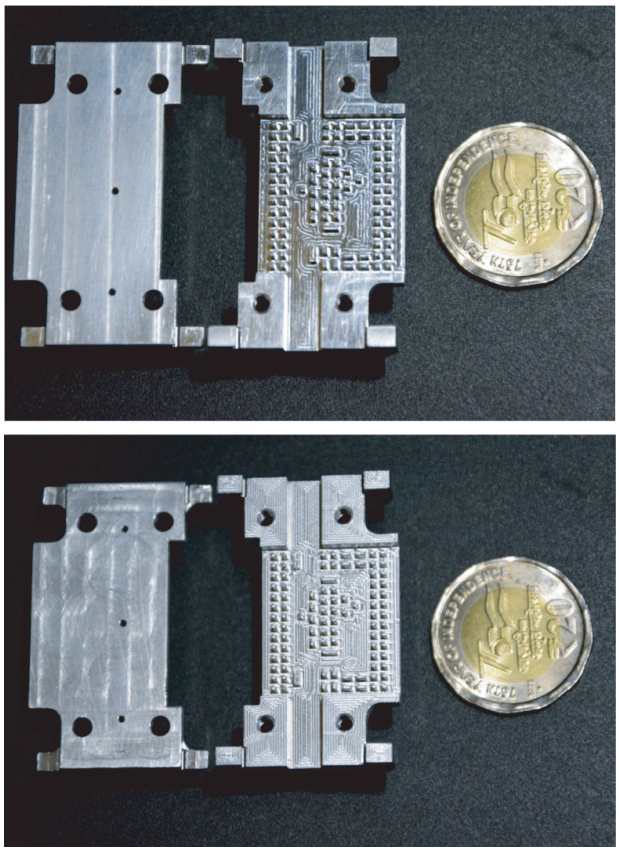

FIGURE 27. Fabricated hardware in open condition. (a) Open condition: old design. (b) Open condition: new design.

tally polarized resonators can be found in [25] but is avoided in this work since the design already has sufficient multipaction margin for space applications.

6. HARDWARE MEASUREMENT

The design reported in [16] and the new design with improved side-lobe imbalance presented in this work have been fabricated with Aluminium metal in the box and cover approach. Fig. 26 shows the fabricated hardware in assembled condition. The

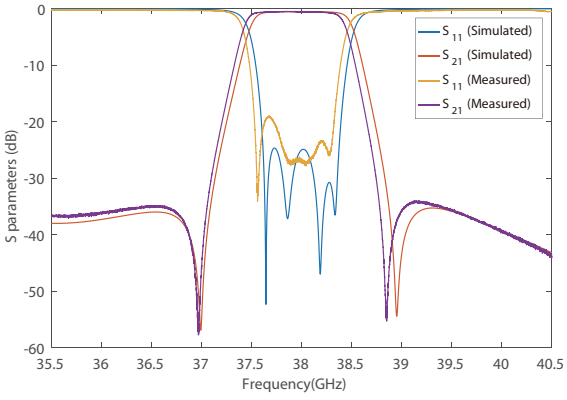

FIGURE 28. EM simulated vs. measured frequency response of the new design with improved sidelobe imbalance.

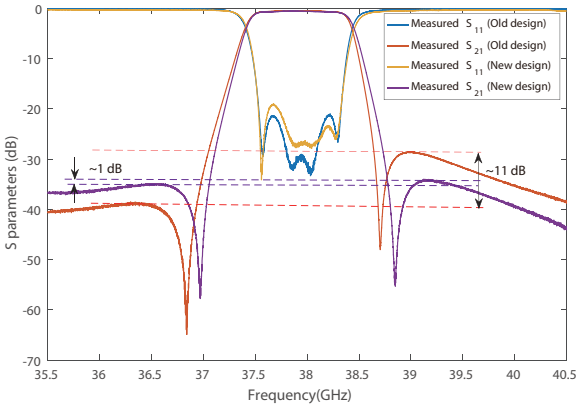

FIGURE 29. Measured frequency response of the old design vs. the new design.

fabricated filters in open condition are shown in Fig. 27. The simulated vs. measured response of the old design is shown in Fig. 4 to demonstrate the sidelobe imbalance issue. The old design is a special case (case 6) in the 6 corner cases studied in this work. The comparison between the EM simulated response and measured hardware response of the new design is shown in Fig. 28. The new design has a sidelobe imbalance of approximately 1 dB. The measured insertion loss in both the cases is around 0.55 dB which can be further improved by silver plating. Both the fabricated filters are slightly shifted in frequency which can be attributed to the fabrication tolerances and can be taken care of in the next iteration of fabrication. The measured frequency responses of the old and new designs are overlaid in Fig. 29 which clearly shows a significant improvement (around 10 dB) in sidelobe imbalance.

7. CONCLUSIONS

A 4-pole quasi-elliptic filter with CQ topology is designed and developed using TE_{102} overmoded cavity resonator in GGW technology and studied systematically in detail to come up with a final design with a very low level of spurious coupling and sidelobe imbalance. The effect of the location of the external coupling structures in the overall spurious coupling level is analyzed in detail to tackle the sidelobe imbalance issue which can be generalized to higher-order filters as well. The designed filter uses all-capacitive irises to ease the fabrication and development process by avoiding any complex coupling structure (for the negative cross-coupling). The designed filter is verified both in full-wave 3-D EM simulation and through hardware measurements. The hardware measurements are consistent and in agreement with the simulation results. In lieu of the minor frequency shift (consistent in both the hardware) which can be attributed to the fabrication tolerances, the return loss is better than 20 dB without using any tuning screws. High-power considerations and frequency drifts due to the space environment are also discussed in detail to explain the design margins in space-based hardware. These overmoded cavity resonator based groove gap waveguide filters with very low sidelobe imbalance can be the potential candidates for the bulk requirements in next-generation high-throughput satellites.

ACKNOWLEDGEMENT

The authors thank Mr. Nilesh M Desai, Director, Space Applications Centre, Mr. D. K. Singh, Associate Director, Mr. Sumitesh Sarkar, Deputy Director, SNPA and Mr. Jayesh Thakkar, Group Director, RFSG for their encouragement in carrying out this work. The authors are also thankful to Mr. E D V Nagesh, Mr. Prajot Anil Ballamwar, Mr. Shivam Tiwari of MFD, Mr. Vineet Kumar Dad of PPCD, and Mr. Ramagiri Santhosh Kumar, Head, AMTD, Space Applications Centre for useful discussions. Lastly, the authors would like to express their gratitude to Mr. Senjam Ibomcha Singh for the technical support, and Mr. Ajay Kumar and Mr. Sumit Dubey from the mechanical design team for their invaluable suggestions and support.

REFERENCES

[1] Kildal, P.-S., E. Alfonso, A. Valero-Nogueira, and E. Rajo-Iglesias, "Local metamaterial-based waveguides in gaps between parallel metal plates," *IEEE Antennas and Wireless Propagation Letters*, Vol. 8, 84–87, 2008.

[2] Kildal, P.-S., "Three metamaterial-based gap waveguides between parallel metal plates for mm/submm waves," in *2009 3rd European Conference on Antennas and Propagation*, 28–32, Berlin, Germany, 2009.

[3] Vicente, C. and H. L. Hartnagel, "Passive-intermodulation analysis between rough rectangular waveguide flanges," *IEEE Transactions on Microwave Theory and Techniques*, Vol. 53, No. 8, 2515–2525, 2005.

[4] Zaman, A. U., P.-S. Kildal, and A. A. Kishk, "Narrow-band microwave filter using high-Q groove gap waveguide resonators with manufacturing flexibility and no sidewalls," *IEEE Transactions on Components, Packaging and Manufacturing Technology*, Vol. 2, No. 11, 1882–1889, 2012.

[5] Kant, R., D. Ghodgaonkar, P. Samanta, V. K. Dad, and P. K. Ambati, "An optimum microwave filter design using groove gap waveguide technology for low-loss high-power applications at Ku and Q-band," in *2023 IEEE Wireless Antenna and Microwave Symposium (WAMS)*, 1–5, Ahmedabad, India, 2023.

[6] Alós, E. A., A. U. Zaman, and P.-S. Kildal, "Ka-band gap waveguide coupled-resonator filter for radio link diplexer application," *IEEE Transactions on Components, Packaging and Manufacturing Technology*, Vol. 3, No. 5, 870–879, 2013.

[7] Zarifi, D. and M. Nasri, "Design of a Ku-band filter based on groove gap waveguide technology," *Progress In Electromagnetics Research Letters*, Vol. 76, 71–76, 2018.

[8] Marini, S., M. Ferrando-Rocher, A. M. Hernández, E. G. Nieves, A. J. López, and V. E. Boria, "Ka-band diplexer design based on half-mode groove gap waveguide," *AEU — International Journal of Electronics and Communications*, Vol. 175, 155062, 2024.

[9] Arezoomand, M., A. Pirhadi, and S. Karimian, "Design and implementation of a Ku-band cross-coupled gap waveguide filter using non-resonating negative coupling node," *IET Microwaves, Antennas & Propagation*, Vol. 12, No. 8, 1345–1351, 2018.

[10] Al-Juboori, B., Y. Huang, D. Klugmann, M. Hussein, and J. Zhou, "Millimeter wave cross-coupled bandpass filter based on groove gap waveguide technology," in *2017 10th UK-Europe-China Workshop on Millimetre Waves and Terahertz Technologies (UCMMT)*, 1–4, Liverpool, UK, 2017.

[11] Rezaee, M. and A. U. Zaman, "Groove gap waveguide filter based on horizontally polarized resonators for V-band applications," *IEEE Transactions on Microwave Theory and Techniques*, Vol. 68, No. 7, 2601–2609, 2020.

[12] Shu, M., W. Wu, Q. Yang, J. Chen, C. Guo, and A. Zhang, "Compact filters based on dual-mode gap waveguide cavities and 3D printing technology," *Microwave and Optical Technology Letters*, Vol. 65, No. 3, 727–732, 2023.

[13] Xiu, T., Y. Yao, H. Jiang, X. Cheng, C. Wang, B. Wang, J. Yu, and X. Chen, "Design of a compact and low-loss E-band filter based on multilayer groove gap waveguide," *IEEE Microwave and Wireless Components Letters*, Vol. 31, No. 11, 1211–1214, 2021.

[14] Farahani, H. S. and W. Bösch, "Ku-band gap waveguide filter with negative coupling structure," in *2019 European Microwave Conference in Central Europe (EuMCE)*, 290–293, Prague, Czech, 2019.

[15] Yao, B., N. Huang, G. Zhang, X. Zhou, J. Lu, K. W. Tam, W. Zhang, and W. Tang, "Dual-band bandpass filter with high selectivity based on 3D printable groove gap waveguide," *IET Microwaves, Antennas & Propagation*, Vol. 17, No. 10, 827–831, 2023.

[16] Kant, R., D. Ghodgaonkar, A. Jindal, P. Samanta, H. Modi, and P. K. Ambati, "Design of a quasi-elliptic filter in groove gap waveguide technology using overmoded cavity for low-loss high-power applications at Q-band," in *2023 IEEE Microwaves, Antennas, and Propagation Conference (MAPCON)*, 1–5, 2023.

[17] Valero-Nogueira, A., E. Alfonso, J. I. Herranz, and P.-S. Kildal, "Experimental demonstration of local quasi-TEM gap modes in single-hard-wall waveguides," *IEEE Microwave and Wireless Components Letters*, Vol. 19, No. 9, 536–538, 2009.

[18] Shaterian, Z., A. K. Horestani, and M. Mrozowski, "Design guidelines for microwave filters in gap waveguide technology," in *2021 IEEE MTT-S International Microwave Filter Workshop (IMFW)*, 182–184, Perugia, Italy, 2021.

[19] Thomas, J. B., "Cross-coupling in coaxial cavity filters-a tutorial overview," *IEEE Transactions on Microwave Theory and Techniques*, Vol. 51, No. 4, 1368–1376, 2003.

[20] Rosenberg, U., "Newplanar'waveguide cavity elliptic function filters," in *1995 25th European Microwave Conference*, Vol. 1, 524–527, 1995.

[21] Cameron, R. J., "General coupling matrix synthesis methods for Chebyshev filtering functions," *IEEE Transactions on Microwave Theory and Techniques*, Vol. 47, No. 4, 433–442, 1999.

[22] Cameron, R. J., "Advanced coupling matrix synthesis techniques for microwave filters," *IEEE Transactions on Microwave Theory and Techniques*, Vol. 51, No. 1, 1–10, 2003.

[23] Ness, J. B., "A unified approach to the design, measurement, and tuning of coupled-resonator filters," *IEEE Transactions on Microwave Theory and Techniques*, Vol. 46, No. 4, 343–351, 1998.

[24] Kudsia, C., K. Ainsworth, and M. Odonovan, "Microwave filters and multiplexing networks for communications satellites in the 1980s," in *8th Communications Satellite Systems Conference*, 522, Orlando, FL, USA, 1980.

[25] Morales-Hernández, A., M. □. Sánchez-Soriano, M. Ferrando-Rocher, S. Marini, M. T. Calduch, and V. E. Boria, "Peak power handling capability in groove gap waveguide filters based on horizontally polarized resonators and enhancement solutions," *IEEE Microwave and Wireless Components Letters*, Vol. 32, No. 7, 859–862, 2022.